

# Candidate Coronagraphic Detections of Protoplanetary Disks around Four Young Stars

J.L. Karr

*Academia Sinica Institute of Astronomy and Astrophysics, PO Box 23-141 Taipei 10617,  
Taiwan, ROC*

N. Ohashi

*Academia Sinica Institute of Astronomy and Astrophysics, PO Box 23-141 Taipei 10617,  
Taiwan, ROC*

T. Kudo

*National Astronomical Observatory of Japan, 2-21-1 Osawa, Mitaka, Tokyo 181-8588,  
Japan*

M. Tamura

*National Astronomical Observatory of Japan, 2-21-1 Osawa, Mitaka, Tokyo 181-8588,  
Japan*

## ABSTRACT

We present potential detections of H-band scattered light emission around four young star, selected from a total sample of 45 young stars observed with the CIAO coronagraph of the Subaru telescope. Two CTTS, CI Tau and DI Cep, and two WTTS, LkCa 14 and RXJ 0338.3+1020 were detected. In all four cases, the extended emission is within the area of the residual PSF halo, and is revealed only through careful data reduction. We compare the observed extended emission with simulations of the scattered light emission, to evaluate the plausibility and nature of the detected emission.

*Subject headings:* stars:protoplanetary disks,stars:pre-main sequence

## 1. Introduction

A well developed picture of the formation of low mass stars has emerged in recent years. Stars form from the collapse of a dense, dusty molecular envelope. As the material collapses,

a circumstellar disk forms around the protostar, through which material is accreted onto the star. At the same time, an outflow propels material out of the envelope. As the star evolves towards the main sequence, the envelope first dissipates, then the optically thick circumstellar disk becomes a thin disk and then a remnant debris disk, over a timescale of approximately 10 Myr. While the general process is well established, the detailed physical processes and time-scales are still an area of active debate. The presence of circumstellar disks is ubiquitous in this picture, and understanding their formation, structure and evolution is a vital step towards understanding the formation of both stars and the planetary systems that form in the disks.

High resolution near-infrared (NIR) coronagraphic observations of scattered light from circumstellar disks have revealed a complex and intriguing variety of disks, ranging from the spiral arm structures of AB Aur (Fukagawa et al. 2004), to tail and ring-like structures around the multiple systems T Tau (Mayama et al. 2006) and GG Tau (Itoh et al. 2002), to butterfly-like scattered light emission from edge-on thick disks in Taurus (Padgett et al. 1999) to the faint debris disks around the relatively evolved sources TW Hya (Krist et al. 2000) and Beta Pic (Heap et al. 2000). A complimentary detection method of particular efficacy in disk studies is the use of imaging polarimetry combined with coronagraphy to observe linearly polarized scattered light from the disk (eg. (Oppenheimer et al. 2008; Perrin et al. 2004; Apai et al. 2004)); a similarly wide variety of morphologies can be seen with this method as well.

Clearly, the complex variety of disks indicates that the processes which shape circumstellar disks are much more complicated than previously thought. There are many factors which can affect the structure of the disk, including the luminosity and multiplicity of the central star, the accretion characteristics, and the age of the disk. In addition, the structure of the disk is intimately connected to the formation of planets, as planetary systems can clear gaps in the disks and the formation of planets can lead to the cessation of accretion onto the star.

Directly resolving the surface of disks in scattered light is a challenging task. In order to observe scattered light on solar system scales, sub-arcsecond resolution is required for even the nearest star forming regions; consequently, either space based observations are required, or a ground based 8 m class telescope with adaptive optics (AO). In addition, the scattered light emission is orders of magnitude less than that of the central star. The stellar light needs to be blocked using a coronagraphic mask, and great care taken in the reduction and analysis of the data to avoid artifacts and false detections.

Relatively few of the vast number of YSOs detected through infrared photometric excess and spectroscopic features have been directly imaged and resolved through infrared coron-

agraphy and polarimetry. A much larger sample of objects is needed to build a consistent picture for the evolution of disk structure. In this paper, we present tentative detections from a large (45 object) sample of young stars which have been observed using the Coronagraphic Imager with Adaptive Optics (CIAO) on the Subaru 8.2 m telescope.

In Section 2 we discuss the observation techniques and sample for the survey. In Section 3 we discuss the details of the data reduction procedure, and the technique used to choose the most robust detections, weeding out instrumental artifacts. We detail the detections and individual sources in Section 4, and discuss the general results in Section 5. In Section 6 we compare the spectral energy distributions (SEDs) and scattered light emission to models and synthetic images, to evaluate the nature and plausibility of the observed emission. The results are summarized in Section 7.

## 2. Observations

### 2.1. Coronagraphic Observations and Scattered Light

The observations presented here are part of a large coronagraphic survey of young stars with the Subaru telescope. This survey had two goals; discovering low luminosity companions to young stars, and directly resolving scattered light from disks in the near-infrared. Near-infrared stellar light scattered from the surface of a circumstellar disk can be a powerful tracer of the morphology and extent of the circumstellar disk, although the interpretation of the results is challenging. Unlike molecular line or sub-mm continuum observations scattered light observations are sensitive to the surface of the disk only, for an optically thick disk, rather than the total amount of material. Consequently, these observations are potentially sensitive to relatively low amounts of material. Conversely, information about the interior of the disk is not probed. An additional complication in interpretation is caused by the fact that scattered light can also be observed from the interior walls of the outflow cavity of embedded young stars, and structures in the envelope itself, leading to confusion regarding the source of the emission.

### 2.2. The Sample

All the imaging data were taken with the Subaru Coronagraphic Imager with Adaptive Optics (Tamura et al. 2000; Murakawa et al. 2004), and were retrieved from the public Subaru archive. The original, full sample of targets was composed of roughly 100 targets selected for the likelihood of observing a disk. The sample was not chosen as a statistically uniform

one; rather, it consists of a selection of sources of various masses and spectral types which show strong evidence for the presence of a circumstellar disk in a variety tracers. Evidence for a circumstellar disk can be inferred from excess emission in the near- to far-infrared (Adams et al. 1988), resulting from the absorption and re-radiation of stellar light by dust, from submillimeter and millimeter line and continuum emission emitted by the molecular gas and dust, infrared spectra showing dust features, and from X-ray emission (particularly for weak-lined T-Tauri stars (WTTS)), H- $\alpha$  and lithium line emission indicative of active accretion, which imply the presence of an associated disk.

A large number of individual sources in the original sample have been analyzed by a variety of researcher, particularly for the higher mass Herbig Ae/Be stars and classical T-Tauri stars with optically thick, more readily observable disks, and those sources which clearly show evidence of extended structure in scattered light (e.g. Fukagawa et al. (2004); Mayama et al. (2006); Hioki et al. (2007); Itoh et al. (2008); Kudo et al. (2008)). The remaining sources, consisting primarily of lower mass K and M stars and more evolved weak lined T-Tauri stars, do not immediately show evidence for scattered light from disks. As a result, careful, detailed data reduction and analysis are required in order to detect extended emission from scattered light. The existence and nature of circumstellar disks around WTTS is still a subject of much debate. This makes the detection of disks around WTTS a less likely proposition; at the same time it makes the detection of such a disk scientifically very significant, and of great interest in furthering the understanding of disk evolution. Therefore, the study of these objects is of great interest in spite of the small amount of material.

In light of this, we have reduced and analyzed forty-five sources from the above survey, in order to detect extended emission on small physical scales ( $< 200$  AU). Table 1 lists all the sources in this sample. This sample is heavily weighted towards lower mass stars, particularly K and M stars, and weak-lined T-Tauri stars. The sample is composed of 12 Classical T Tauri stars (CTTS), 31 weak line T Tauri stars, 1 Herbig Be star and 1 YSO. The spectral types are weighted towards lower mass stars; 8 M stars, 24 K stars, 7 G stars, 1 F star and three stars of unknown spectral type. Most of the sources are located in Taurus, at a distance of 140 pc, while a few are located in other regions. The complete 45 object sample, with detection limits and companions, will be presented in a subsequent paper.

Near-infrared coronagraphic observations in H-band were performed on 13 nights between November 2003 and November 2005. The observing times and number of frames used vary from source to source, and are listed in Table 2. Even with the use of a coronagraphic mask, there is still significant remnant flux in the wings of the point spread function (PSF). Consequently, reference PSFs from non-binary, non-disk sources were observed for each target, in order to produce the near-complete post observation subtraction of the PSF.

Photometric standards from the UKIRT faint spectral standard catalogue (Leggett et al. 2006) were observed on each night.

### 3. Data Reduction

#### 3.1. Basic Reduction

The data were reduced using the standard IRAF routines; dark frame subtraction, flat fielding, bad pixel masking, cosmic ray reduction and sky subtraction. The position of the source in the image can shift slightly due to minor variations in the adaptive optics performance during the night. The partial transparency of the CIAO mask ( $\approx 2\%$ ) means that the central source is visible through the mask. Consequently, the position of the central source can be used to center each frame exactly. The target frames were checked for AO performance, using a measure of the AO quality which compares the peak flux to the flux in the wings, measuring the sharpness of the image. Each target and reference frame was visually inspected, to check for bad frames, mis-aligned PSFs or other issues.

For each target source, the ten frames with the best adaptive optics were selected. Ten PSF reference frames were then selected to best match the quality of the adaptive optics in the target source. The reference frames were rotated to match the instrumental rotation of each target frame, aligning the spider patterns on the image. The reference frames were then co-added to create a reference PSF for each individual target frame.

There are several possible methods for determining the best parameters for the subtraction of the reference frame, which may need to be shifted slightly in position (due to the centering of the source within the mask), and/or scaled to match the intensity of the target frame. We have adopted a two phase approach; an automated routine, followed by a manual fine-tuning. In the first phase, the averaged intensity in the wings of the PSF was used to estimate the scaling factor. The shift in the position of the central pixel was determined by calculating the noise in the wings of the PSF and minimizing the difference between the noise at four positions located away from the diffraction spikes. In the second phase, we interactively checked the parameters derived above, to test for the quality of the fit and the robustness of the parameters. It should be noted that the automated algorithm will work best in the absence of any extended emission, and will result in over-subtraction for symmetric extended emission. At this point, corrections to the position and scaling were generally minor, typically less than a few pixel in position and 10% in scaling. The final subtracted images were then co-added to produce a final image.

PSF subtraction for binary sources is a more complex process. In this case, a reference

PSF was created by adding two PSFs, each scaled and shifted to match the relative fluxes at positions of the binary components, before subtraction.

### 3.2. Detecting Extended Emission

Potential detections were selected through a multi-stage process. Only one source, Haro 6-10, showed clear extended emission in the original coronagraphic image, as is the typical case in coronagraphic detections of extended emission from disks and outflows. Haro 6-10 is a known embedded binary protostar, and the detected emission is not likely to be disk emission, but rather scattered light off the interior of the outflow cavity (Koresko et al. 1999). For the remaining sources, potential detections were limited to the region within the radius of the PSF halo. As a consequence, the quality of the final subtraction is in large part determined by the fine details of the AO quality in the images, and the matching of the target and reference PSFs prior to subtraction. Subtraction artifacts are therefore of major concern.

The detectability of scattered light from the surface of disks depends on the brightness of the scattered light, the orientation and morphology of the disk, and the distance of the source. The coronagraphic observations are also highly dependent on the technical details of the observations. The coronagraphic mask size determines the minimum angular scale at which scattered light can be detected; this is in practice larger than the mask size. The quality of the data is also highly sensitive to the performance of the adaptive optics system and the subtraction of the residual PSF effects. Even with the selection of the best quality image frames there are noticeable variations in the size of the PSF. Poor AO performance and mis-matched PSFs can either mask existing emission or create false detections. For sources which show extended emission outside of the area dominated by the PSF halo, as in most previously reported cases, this makes the selection of the best PSF subtraction parameters problematic. For extended emission that is contained entirely within the halo dominated region, as in the sample presented here, the uncertainty comes in at the detection level, rather than the interpretation level.

A source was rejected if it showed a good but negative PSF subtraction, in which there was no residual extended emission or remaining artifacts. A source was also rejected if it showed a poor but negative PSF subtraction, with no remnant extended emission but significant artifacts from the subtraction process. Figure 1 shows an example of a rejected subtraction; DF Tau is the result of a null result from a moderately bright source. The inner region of the subtraction, immediately outside the mask, is dominated by subtraction artifacts and is useless for the purposes of data analysis, even in example of clear detec-

tions. In practice, subtraction artifacts from the diffraction spikes remain even in the best subtractions and for bright sources in particular, these are impossible to remove completely. In Figure 2 we show the pre and post-PSF subtraction profile for the same source, more quantitatively illustrating the magnitude of the halo subtraction effect; compare with the detection profiles discussed in Section 4. If a source showed evidence of extended emission, it was rejected unless the extended emission was present with the same morphology and direction in all ten of the individual frames.

We performed a series of tests on potential detections to attempt to rule out instrumental or subtraction artifacts. We checked the variation of the PSF from frame to frame by eye; a visible variation in PSF size was noticeable in most observation runs, but a distortion in the shape of the PSF was not readily apparent. A rotation of the reference source by 90 degrees before subtraction was in general inconclusive; small scale emission was dominated by the effects of the diffraction spikes. When possible, we tested variations in the individual reductions to check the robustness of the subtraction.

In addition, we checked for systematic effects in the observational data and processing which could explain the detected sources. We compared the relative rotations of the target and reference, the brightness of the sources, and the quality of the PSF matching between the target and reference source. The potential detections did not show any systematic biases when compared to the rest of the sample, in relative rotation angle, flux of the source, quality of the PSF matching or night observed.

The profile of the extended emission was calculated, and compared to the profile from known bad subtraction artifacts. This was also relatively inconclusive, due to the small angular scale over which extended emission was observed.

## 4. Results

At the end of the above process we retained four potential detections (excluding Haro 6-10). Each detection, in itself, is marginal; it is the large number of comparison non-detections in this sample which indicates that they are of interest and worthy of subsequent, confirming observations. There are two CTTS, CI Tau (located in Taurus) and DI Cep (at a distance of 300 pc), and two WTTS, LkCa 14 and RXJ 0338.3+1020, both in Taurus. CI Tau, DI Cep and LkCa 14 all show nebulous emission that is extended along one axis, while RXJ 0338.3+1020 shows more symmetric emission.

Table 3 lists the physical of the potential detections; position, spectral type, YSO class, distance, binarity and presence of a companion in the field of view, detection limits of the observations, and morphology and scale of the extended emission. Figure 3 shows pre- and post-subtraction images for the detections. The central region, dominated by subtraction artifacts, has been manually masked. In the subtracted image the region dominated by the diffraction spikes has also been masked for interpretive purposes. Figure 4 shows the corresponding profiles. In the left panel, the pre- and post-subtraction profiles are compared, while in the right panel the profiles along the major axis of emission and perpendicular to it are shown. In all cases the profiles are averaged over seven pixels in width. When compared with the non-detection profiles of Figure 2, it can be seen that the the extended emission is much stronger and more extended along the major axis of the detections than along the minor axis or the non-detections. The magnitude of the residual PSF emission, compared to the detected emission, is also clearly seen, and the need for careful PSF subtraction.

#### 4.1. CI Tau

CI Tau is a classical T-Tauri star of type K7, located in the Taurus region at a distance of 140 pc (Kenyon and Hartmann 1995). The post-subtraction image of CI Tau in Figure 3 shows a nebulosity extending from NE to SW. To the south-west there is some contamination from a ghost image in the target frame, which has been labeled. The physical extent of the nebulosity is approximately 190 AU, and the position angle 145 degrees east of north.

There have been previous resolved detections of the circumstellar disk around CI Tau. Dutrey et al. (1996), in 2.7 mm continuum observations with the Plateau de Bure interferometer, made a marginal resolution of the disk, with an extent of 2.0 by 0.8 arcseconds and a position angle of 40 degrees. Later interferometric sub-mm observations performed by Andrews and Williams (2007) at 340 GHz with the SMA resolved emission. They fit a disk with a radius of 225 AU, a mass of  $0.04 M_{\odot}$ , an inclination of 46 degrees and a position angle of 131 degrees, nearly perpendicular to the previous detection. It should be noted that these observations were barely resolved. The latter angle is consistent with the major axis of our NIR scattered disk, in which case the scattered light images might show the light from the surface of the disk detected with SMA.



## 4.2. DI Cep

DI Cepheus is a CTTS with a spectral type of G8, located at a distance of 300 pc (Gameiro et al. 2006). We detect a nebulosity, shown in the second two panels of Figure 3, that is similar in morphology to CI Tau, although the greater distance gives a physical scale of 370 AU for DI Cep. The position angle is 95 degrees. A companion candidate can be seen to the south east of the image.

There have been no high resolution observations at the scales probed by the Subaru observations. The strong infrared excess in the SED (discussed further in Section 6.1), is strongly indicative of extensive circumstellar material, while the  $H\alpha$  line width (Hessman and Guenther 1997) implies accretion, which assumes the presence of a disk. Mid infrared spectroscopy by Bowey et al. (2003) detected strong silicate emission from circumstellar dust; they fit a disk with a  $10^4$  AU radius to the line profile. Gameiro et al. (2006) performed high resolution optical spectroscopy of DI Cep, and argue that its disk is observed nearly edge on. The morphology of the scattered light images indicate a disk that is seen at an angle from face on, although not likely directly edge on.

## 4.3. LkCa 14

LkCa 14 (aka V1115 Tau) is a weak-lined T-Tauri source with a spectral type of M0V, also located in the Taurus region (Kenyon and Hartmann 1995). The extended emission shown in the third set of panels in Figure 3 is of smaller scale than the other sources, and as a result it is the weakest of our detections. The emission is again elongated, with a physical radius of 120 AU and a position angle of 135 degrees. The corresponding profiles are shown in the third panel of Figure 4.

There has been no previous, resolved detection of the disk around LkCa 14. Andrews and Williams (2005) place an upper limit on the mass of the disk of  $0.004 M_{\odot}$ , based on single dish sub-mm observations at 340 GHz.  $H\alpha$  is seen in emission, which is an indication of accretion, and indirectly of the presence of circumstellar material. It should be noted that coronagraphic observations probe scattered light off the surface of the disk, and consequently a relatively small amount of material is needed to produce a scattered light image.

#### 4.4. RXJ 0338

RX J0338 is a weak-line T-Tauri star of type G9, also located in Taurus at 140 pc (Magazzu et al. 1997). It shows irregular extended emission, as seen in the last two panels of Figure 3, with a radius of 190 AU. Very little is known about this X-ray selected source.

### 5. General Discussion

The detections reported above are tenuous ones; it is only the large scale nature of the survey and the comparison with multiple non-detections that allows us to select these as interesting sources for follow-up observations. One clear result from the analysis of these data is the strong dependence of the results on the quality of the adaptive optics performance. Consequently, these sources are likely best viewed as the most promising candidates for subsequent observations, rather than as firm detections. Further observations with more advanced coronagraphic and adaptive optics (particularly HICIAO and the new 188 element adaptive optics system at Subaru (Hodapp et al. 2008)) are in the planning stages, while observations at longer wavelengths could probe the inner disk material, and ideally provide velocity information to determine the disk orientation and provide an independent comparison to the infrared morphology.

Of the four sources shown here, three show elongated structures, while one shows more circularly symmetric structure. In addition to light scattered from the surface of the disk, light may also be scattered from the interior walls of an outflow cavity; with single wavelength data it can be difficult, if not impossible, to distinguish between light from a small scale outflow cavity and an inclined disk. Further data are needed. However, it should be observed that of the three elongated features, one is a weak line T-Tauri star, which should not show any significant outflow activity. Even the classical T-Tauri stars should have a relatively minor envelope compared to the earlier phases of star formation; this is supported by the optical visibility of the sources. The emission is also relatively symmetric about the central star. In the case of an outflow cavity, sources are rarely observed face on, and therefore the red-shifted lobe is generally more highly extinguished than the blue-shifted one, due to the geometry of the system. Both of these observations argue against an outflow cavity interpretation for these objects.

The detections around the WTTS are, if confirmed, of great interest. The nature and extent (or even presence) of disks around the more evolved WTTS are not well constrained, and the small amounts of material involved make observations in the mm or sub-mm difficult. Consequently, a positive detection of a disk around a WTTS will have very interesting

implications for the long term evolution of circumstellar disks.

The disk properties and frequency of WTTS are not well constrained, either by observation or by theory. The disks themselves are low mass and consequently low luminosity. From a theoretical perspective, the disk dissipation timescale is of importance, and also not well constrained. Ground based photometry is not sufficient for the detection of WTTS disks in the infrared, and earlier space missions such as ISO and IRAS were not of sufficient sensitivity, due to the small excesses at longer wavelengths and the photospheric SEDs at shorter wavelengths. Post Spitzer statistics for infrared derived WTTS disk fractions vary considerably, from 30-35% for WTTS in star forming clusters (Lada et al. 2006; Sicilia-Aguilar et al. 2006; Padgett et al. 2006), to 23% for WTTS in the Taurus region (Cieza et al. 2007), to 6% for the areas surrounding star forming regions (Padgett et al. 2006). Sub-mm studies of well known sources have derived disk fractions for WTTS (with masses in the range of  $10^{-1}$  to  $10^{-3} M_{\odot}$ ) of 10% (Osterloh and Beckwith 1995; Andrews and Williams 2005).

From these recent studies it is clear that a substantial minority of WTTS have remnant circumstellar disks. This is an encouraging result for further, more sensitive, coronagraphic studies, as a relatively small amount of material is necessary to produce scattered light images. One area of uncertainty, however, is the scattering properties of the dust around WTTS. For a WTTS, planetary formation and the fragmentation of planetesimals will strongly shape the dust properties. Even at earlier phases, dust settling and coalescence are also expected to alter the scattering and emission properties of the disk. A WTTS disk with significantly processed dust, and consequently much larger average grain size, might result in a significantly fainter scattered light image for a given disk mass. Further, longer wavelength observations are needed for the sources in this paper to further constrain their disk properties.

## 6. Constraining the Disks

Given the tenuous nature of the above detections, it is important to look at the plausibility of the detections from the perspective of the physical size and mass of the potential disks. There are several ways this question can be approached. The photometry of the sources can be used to explore the range of potential disk parameters which are consistent with the shape of the SED. Scattered light images generated from radiative transfer models can be used to probe the nature of the scattered light emission for different disk configurations.

### 6.1. SEDs and Disk Parameters

A team associated with the Spitzer GLIMPSE Legacy survey (Robitaille et al. 2006, 2007) has developed a powerful online tool for fitting SEDs to photometric observations of YSOs, making it possible to efficiently analyze SEDs in the context of physical models of YSO systems. Fitting detailed YSO models to an SED using radiative transfer simulations is a non-trivial task. The group takes a novel approach; first generating a suit of 20,000 3-D radiative transfer models (Whitney et al. 2003b,a) for a grid of 2-D YSO models, using a Monte-Carlo technique which traces the path of individual photons. The models cover a wide range of stellar masses and ages, masses and geometries for disks, envelopes and outflow cavities, and a set of ten inclinations for each model. Observed SEDs, from the optical to millimeter, are then fitted to the grid of models, with the addition of distance and interstellar extinction effects.

There are several important caveats to this method of fitting. The most important is the degeneracy of the fits. With the large number of physical parameters input to the radiative transfer model, the fits are highly non-unique, with multiple combinations of parameters fitting a given SED. Consequently, care must be taken not to over-interpret the physical significance of the results. However, the fits can be used to interpret the plausibility of a given set of models, and to constrain the general best fit of given a parameter. This works better for some parameters than others; the disk inclination, in particular, is poorly constrained by the SED fits.

Figure 5 shows the SEDs and fits for the tentative detections. In each case, we have used the best literature photometry available (optical, near- to far-infrared and sub-mm/mm); the photometry is summarized in Table 4. The distance and interstellar extinction have been constrained to measured values in the initial fit. From the suite of models which result, we have then selected the best model which matches the stellar mass of our source.

CI Tau and DI Cep both show strong infrared excesses in the mid-infrared and beyond. CI Tau is fit with a  $0.4 M_{\odot}$  star with a  $0.03 M_{\odot}$  disk, similar to observational estimates of the disk mass, while DI Cep is fit with a  $1.1 M_{\odot}$  central star, with a disk mass of  $0.03 M_{\odot}$ .

LkCa 14 and RXJ 0338, on the other hand, are adequately fitted by an extinguished stellar spectrum in the range of the available photometry. This is consistent with their classifications as WTTS, where little, if any, infrared excess is generally seen. They do not, therefore, have a large disk, but the SEDs do not rule out the possibility of a low mass remnant disk, or a cooler disk at larger radii with a central gap. The latter would show an excess only at longer wavelengths. The model for LkCa 14 shown is for a  $0.4 M_{\odot}$  star with a disk of  $2.1 \times 10^{-4} M_{\odot}$ , within the observational limits, while RXJ shows a photospheric SED for a central star

of 5600 K, the best fit stellar spectrum.

## 6.2. Modeling the Extended Emission

For further analysis of the morphology of the NIR emission, the scattered light properties of the above SED models can be determined. The radiative transfer codes used for generating the suite of models may be downloaded by the user and run directly. This generates multi-wavelength images that can be directly compared with high resolution observations, after convolution with the relevant instrument parameters.

For the purposes of this paper, we have used the SEDs fit using this technique, as discussed previously in Section 6.1, as input to the radiative transfer code to generate high resolution images. It is important to note that this is not a fit to the images; rather this allows us to explore how probable our observed images are given the source SED and reasonable system geometries. Several appropriate disk models were tested, to explore the range of emission parameters for the given SED. The inclinations, which are poorly constrained by the SEDs but strongly affect the morphology of the scattered light emission, were tuned to match the morphology of the extended emission.

The results for CI Tau are shown in Figure 6 for a model with a total disk mass of  $0.03 M_{\odot}$ , outer radius of 133 AU and a disk inclination of 63 degrees, matching the observed extinction and distance of the source. To compare with the observed data, a mask has been manually added to the images where the coronagraphic mask and diffraction spikes would dominate the image in real data, and the central few pixels (containing the stellar flux) have been removed. The simulated image has then been convolved with an approximation of the Subaru PSF, measured within the coronagraphic mask, and background noise added to match the final co-added image. The extent, morphology and surface brightness of the observed extended emission can be reproduced with a physical disk/star model that is consistent with the observed SED. The flux levels match approximately, although the model levels are lower (by 50%) than the observed values. The physical scales are similar; however the emission in the model drops off abruptly when the edge of the disk is reached, while the observed emission tapers off more gradually.

For the WTTS, the situation is more difficult, as the observed SED only covers the stellar photosphere portion of the spectrum, with no observed excess emission. Therefore, fitting the disk portion of the SED is not possible. However, there are some limits on the parameters of the disk, as an infrared excess is not seen at NIR wavelengths. For RXJ 0338, we ran the SED fitter to produce a suite of consistent models; typically low mass disks

with a central hole. We selected several SED models which matched the central source, and calculated the corresponding scattered light images. Figure 7 shows an image for a disk which is consistent with the observed SED. The model has a disk mass of  $2.8 \times 10^{-3} M_{\odot}$ , with an inner disk gap of 20 AU and an inclination of 41 degrees.

One area of uncertainty in the calculation of the scattered light images is the dust emission characteristics, as the radiative transfer code does not accurately model the dust properties expected for a highly evolved disk. The original models used in the SED fits were generated using dust emission properties derived from the ISM (Whitney et al. 2003b). Calculating the scattered light properties with the same disk geometry and mass, but using the alternate dust models provided with the code (Cotera et al. 2001; Wood et al. 2002; Whittet et al. 2001) does produce a noticeable difference in the scattered light properties, with a variation of about 50% in the size of the disk, measured at a given surface brightness level.

## 7. Summary

We have presented four potential detections from a large (45 object) coronagraphic study of YSOs observed with the Subaru telescope. The detections are marginal, but have been extensively tested for the robustness of the detection against the non-detections in the the sample.

Two of the detections, CI Tau and DI Cep, are CTTS with extensive infrared excesses; the disk around CI Tau has been previous resolved in the sub-mm. Both sources show elongated emission indicative of an inclined disk, CI Tau with a physical radius of 190 AU, the more distant DI Cep with a physical radius of 370 AU. The remaining two detections, RXJ 0338 and LkCa 14, are WTTS and have no previous direct detection of the disks. RXJ 0338 shows roughly symmetrical emission with a radius of 190 AU, while LkCa 14 shows elongated emission with a radius of 120 AU. The WTTS detections, if confirmed, are of great interest, as the nature and frequency of disks around WTTS are not well constrained.

We have fit the SEDs of the sources using the SED fitter of Robitaille et al. (2006), and used several of the resulting fits as input to the companion radiative transfer code. The general morphology and brightness of the scattered light emission from the CTTS can be reproduced with a radiative transfer model of a disk system that is consistent with the optical to mm SED. The calculation of scattered light emission for these sources is harder to constrain, as the observed SEDs do not extend to long enough wavelengths to detect the infrared excess. However, the general morphology of the emission can be reproduced using

a disk model that does not contradict the observed portion of the SED.

Further observations are needed to confirm these detections, in particular future coronagraphic studies. For the WTTS, detections of the infrared excess at longer wavelengths will provide a constraint on the nature of the surrounding disk.

## 8. Appendix A: Reduction Details

The following section contains details of the reduction process primarily of interest to readers with experience in the processing of coronagraphic data.

Figures 8 and 9 shows details of the source rejection pipeline for a source which passes the tests, and for a source which fails the process on several counts. Each sub-image shows the result of a single subtraction, before co-adding. For all the sources, the final subtractions were inspected by eye, in sequence. The final images shown in this paper are the coadded results of the individual frames, with diffraction spikes and central region manually masked.

Figure 8 shows the details of the data reduction for CI Tau. This source passes the detection as extended emission appears in all ten frames, with the morphology and extend similar in all frames; note that there are still some variations in brightness resulting from the subtraction process. In the case of randomly fluctuations in the atmosphere or performance of the adaptive optics, such a coherence in the morphology from frame to frame would not be expected.

Figure 9 shows a source which was initially flagged as possibly showing extended emission, but which later fails the sequence test. Extended emission is not present in half of the best frames, and sources which do show extended emission vary in mophology from frame to frame. Therefore the source is rejected as a likely residual.



## REFERENCES

- Adams, F. C., Shu, F. H., and Lada, C. J.: 1988, *ApJ* **326**, 865
- Andrews, S. M. and Williams, J. P.: 2005, *ApJ* **631**, 1134
- Andrews, S. M. and Williams, J. P.: 2007, *ApJ* **659**, 705
- Apai, D., Pascucci, I., Brandner, W., Henning, T., Lenzen, R., Potter, D. E., Lagrange, A., and Rousset, G.: 2004, *A&A* **415**, 671
- Audard, M., Briggs, K. R., Grosso, N., Güdel, M., Scelsi, L., Bouvier, J., and Telleschi, A.: 2007, *A&A* **468**, 379
- Beichman, C. A., Neugebauer, G., Habing, H. J., Clegg, P. E., and Chester, T. J. (eds.): 1988, *Infrared astronomical satellite (IRAS) catalogs and atlases. Volume 1: Explanatory supplement*, Vol. 1
- Bowey, J. E., Adamson, A. J., and Yates, J. A.: 2003, *MNRAS* **340**, 1173
- Cieza, L., Padgett, D. L., Stapelfeldt, K. R., Augereau, J.-C., Harvey, P., Evans, II, N. J., Merín, B., Koerner, D., Sargent, A., van Dishoeck, E. F., Allen, L., Blake, G., Brooke, T., Chapman, N., Huard, T., Lai, S.-P., Mundy, L., Myers, P. C., Spiesman, W., and Wahhaj, Z.: 2007, *ApJ* **667**, 308
- Cotera, A. S., Whitney, B. A., Young, E., Wolff, M. J., Wood, K., Povich, M., Schneider, G., Rieke, M., and Thompson, R.: 2001, *ApJ* **556**, 958
- Cutri, R. M., Skrutskie, M. F., van Dyk, S., Beichman, C. A., Carpenter, J. M., Chester, T., Cambresy, L., Evans, T., Fowler, J., Gizis, J., Howard, E., Huchra, J., Jarrett, T., Kopan, E. L., Kirkpatrick, J. D., Light, R. M., Marsh, K. A., McCallon, H., Schneider, S., Stiening, R., Sykes, M., Weinberg, M., Wheaton, W. A., Wheelock, S., and Zacarias, N.: 2003, *2MASS All Sky Catalog of point sources*, The IRSA 2MASS All-Sky Point Source Catalog, NASA/IPAC Infrared Science Archive. <http://irsa.ipac.caltech.edu/applications/Gator/>
- Dutrey, A., Guilloteau, S., Duvert, G., Prato, L., Simon, M., Schuster, K., and Menard, F.: 1996, *A&A* **309**, 493
- Egan, M. P., Price, S. D., Shipman, R. F., Gugliotti, G. M., Tedesco, E. F., Moshir, M., and Cohen, M.: 1999, in M. D. Bica, R. M. Cutri, and B. F. Madore (eds.), *Astrophysics with Infrared Surveys: A Prelude to SIRTF*, Vol. 177 of *Astronomical Society of the Pacific Conference Series*, pp 404–+

- Fukagawa, M., Hayashi, M., Tamura, M., Itoh, Y., Hayashi, S. S., Oasa, Y., Takeuchi, T., Morino, J.-i., Murakawa, K., Oya, S., Yamashita, T., Suto, H., Mayama, S., Naoi, T., Ishii, M., Pyo, T.-S., Nishikawa, T., Takato, N., Usuda, T., Ando, H., Iye, M., Miyama, S. M., and Kaifu, N.: 2004, *ApJ* **605**, L53
- Furlan, E., Hartmann, L., Calvet, N., D’Alessio, P., Franco-Hernández, R., Forrest, W. J., Watson, D. M., Uchida, K. I., Sargent, B., Green, J. D., Keller, L. D., and Herter, T. L.: 2006, *ApJS* **165**, 568
- Gameiro, J. F., Folha, D. F. M., and Petrov, P. P.: 2006, *A&A* **445**, 323
- Grankin, K. N., Bouvier, J., Herbst, W., and Melnikov, S. Y.: 2008, *A&A* **479**, 827
- Hartmann, L., Megeath, S. T., Allen, L., Luhman, K., Calvet, N., D’Alessio, P., Franco-Hernandez, R., and Fazio, G.: 2005, *ApJ* **629**, 881
- Heap, S. R., Lindler, D. J., Lanz, T. M., Cornett, R. H., Hubeny, I., Maran, S. P., and Woodgate, B.: 2000, *ApJ* **539**, 435
- Hessman, F. V. and Guenther, E. W.: 1997, *A&A* **321**, 497
- Hioki, T., Itoh, Y., Oasa, Y., Fukagawa, M., Kudo, T., Mayama, S., Funayama, H., Hayashi, M., Hayashi, S. S., Pyo, T.-S., Ishii, M., Nishikawa, T., and Tamura, M.: 2007, *AJ* **134**, 880
- Hodapp, K. W., Suzuki, R., Tamura, M., Abe, L., Suto, H., Kandori, R., Morino, J., Nishimura, T., Takami, H., Guyon, O., Jacobson, S., Stahlberger, V., Yamada, H., Shelton, R., Hashimoto, J., Tavrov, A., Nishikawa, J., Ukita, N., Izumiura, H., Hayashi, M., Nakajima, T., Yamada, T., and Usuda, T.: 2008, in *Society of Photo-Optical Instrumentation Engineers (SPIE) Conference Series*, Vol. 7014 of *Presented at the Society of Photo-Optical Instrumentation Engineers (SPIE) Conference*
- Ismailov, N. Z. and Grankin, K. N.: 2007, *Astronomy Letters* **33**, 113
- Itoh, Y., Hayashi, M., Tamura, M., Oasa, Y., Hioki, T., Fukagawa, T., and Kudo, T.: 2008, *PASJ* **60**, 223
- Itoh, Y., Tamura, M., Hayashi, S. S., Oasa, Y., Fukagawa, M., Kaifu, N., Suto, H., Murakawa, K., Doi, Y., Ebizuka, N., Naoi, T., Takami, H., Takato, N., Gaessler, W., Kanzawa, T., Hayano, Y., Kamata, Y., Saint-Jacques, D., and Iye, M.: 2002, *PASJ* **54**, 963
- Kenyon, S. J. and Hartmann, L.: 1995, *ApJS* **101**, 117

- Koresko, C. D., Blake, G. A., Brown, M. E., Sargent, A. I., and Koerner, D. W.: 1999, *ApJ* **525**, L49
- Krist, J. E., Stapelfeldt, K. R., Ménard, F., Padgett, D. L., and Burrows, C. J.: 2000, *ApJ* **538**, 793
- Kudo, T., Tamura, M., Kitamura, Y., Hayashi, M., Kokubo, E., Fukagawa, M., Hayashi, S. S., Ishii, M., Itoh, Y., Mayama, S., Momose, M., Morino, J., Oasa, Y., Pyo, T.-S., and Suto, H.: 2008, *ApJ* **673**, L67
- Lada, C. J., Muench, A. A., Luhman, K. L., Allen, L., Hartmann, L., Megeath, T., Myers, P., Fazio, G., Wood, K., Muzerolle, J., Rieke, G., Siegler, N., and Young, E.: 2006, *AJ* **131**, 1574
- Leggett, S. K., Currie, M. J., Varricatt, W. P., Hawarden, T. G., Adamson, A. J., Buckle, J., Carroll, T., Davies, J. K., Davis, C. J., Kerr, T. H., Kuhn, O. P., Seigar, M. S., and Wold, T.: 2006, *MNRAS* **373**, 781
- Magazzu, A., Martin, E. L., Sterzik, M. F., Neuhauser, R., Covino, E., and Alcalá, J. M.: 1997, *A&AS* **124**, 449
- Mayama, S., Tamura, M., Hayashi, M., Itoh, Y., Fukagawa, M., Suto, H., Ishii, M., Murakawa, K., Oasa, Y., Hayashi, S. S., Yamashita, T., Morino, J., Oya, S., Naoi, T., Pyo, T.-S., Nishikawa, T., Kudo, T., Usuda, T., Ando, H., Miyama, S. M., and Kaifu, N.: 2006, *PASJ* **58**, 375
- Monet, D. G., Levine, S. E., Canzian, B., Ables, H. D., Bird, A. R., Dahn, C. C., Guetter, H. H., Harris, H. C., Henden, A. A., Leggett, S. K., Levison, H. F., Luginbuhl, C. B., Martini, J., Monet, A. K. B., Munn, J. A., Pier, J. R., Rhodes, A. R., Riepe, B., Sell, S., Stone, R. C., Vrba, F. J., Walker, R. L., Westerhout, G., Brucato, R. J., Reid, I. N., Schoening, W., Hartley, M., Read, M. A., and Tritton, S. B.: 2003, *AJ* **125**, 984
- Murakawa, K., Suto, H., Tamura, M., Kaifu, N., Takami, H., Takato, N., Oya, S., Hayano, Y., Gaessler, W., and Kamata, Y.: 2004, *PASJ* **56**, 509
- Oppenheimer, B. R., Brenner, D., Hinkley, S., Zimmerman, N., Sivaramakrishnan, A., Soumerai, R., Kuhn, J., Graham, J. R., Perrin, M., Lloyd, J. P., Roberts, Jr., L. C., and Harrington, D. M.: 2008, *ApJ* **679**, 1574
- Osterloh, M. and Beckwith, S. V. W.: 1995, *ApJ* **439**, 288

- Padgett, D. L., Brandner, W., Stapelfeldt, K. R., Strom, S. E., Terebey, S., and Koerner, D.: 1999, *AJ* **117**, 1490
- Padgett, D. L., Cieza, L., Stapelfeldt, K. R., Evans, II, N. J., Koerner, D., Sargent, A., Fukagawa, M., van Dishoeck, E. F., Augereau, J.-C., Allen, L., Blake, G., Brooke, T., Chapman, N., Harvey, P., Porras, A., Lai, S.-P., Mundy, L., Myers, P. C., Spiesman, W., and Wahhaj, Z.: 2006, *ApJ* **645**, 1283
- Perrin, M. D., Graham, J. R., Kalas, P., Lloyd, J. P., Max, C. E., Gavel, D. T., Pennington, D. M., and Gates, E. L.: 2004, *Science* **303**, 1345
- Robitaille, T. P., Whitney, B. A., Indebetouw, R., and Wood, K.: 2007, *ApJS* **169**, 328
- Robitaille, T. P., Whitney, B. A., Indebetouw, R., Wood, K., and Denzmore, P.: 2006, *ApJS* **167**, 256
- Sicilia-Aguilar, A., Hartmann, L., Calvet, N., Megeath, S. T., Muzerolle, J., Allen, L., D’Alessio, P., Merín, B., Stauffer, J., Young, E., and Lada, C.: 2006, *ApJ* **638**, 897
- Tamura, M., Suto, H., Itoh, Y., Ebizuka, N., Doi, Y., Murakawa, K., Hayashi, S. S., Oasa, Y., Takami, H., and Kaifu, N.: 2000, in M. Iye and A. F. Moorwood (eds.), *Society of Photo-Optical Instrumentation Engineers (SPIE) Conference Series*, Vol. 4008 of *Presented at the Society of Photo-Optical Instrumentation Engineers (SPIE) Conference*, pp 1153–1161
- Whitney, B. A., Wood, K., Bjorkman, J. E., and Cohen, M.: 2003a, *ApJ* **598**, 1079
- Whitney, B. A., Wood, K., Bjorkman, J. E., and Wolff, M. J.: 2003b, *ApJ* **591**, 1049
- Whittet, D. C. B., Gerakines, P. A., Hough, J. H., and Shenoy, S. S.: 2001, *ApJ* **547**, 872
- Wood, K., Wolff, M. J., Bjorkman, J. E., and Whitney, B.: 2002, *ApJ* **564**, 887

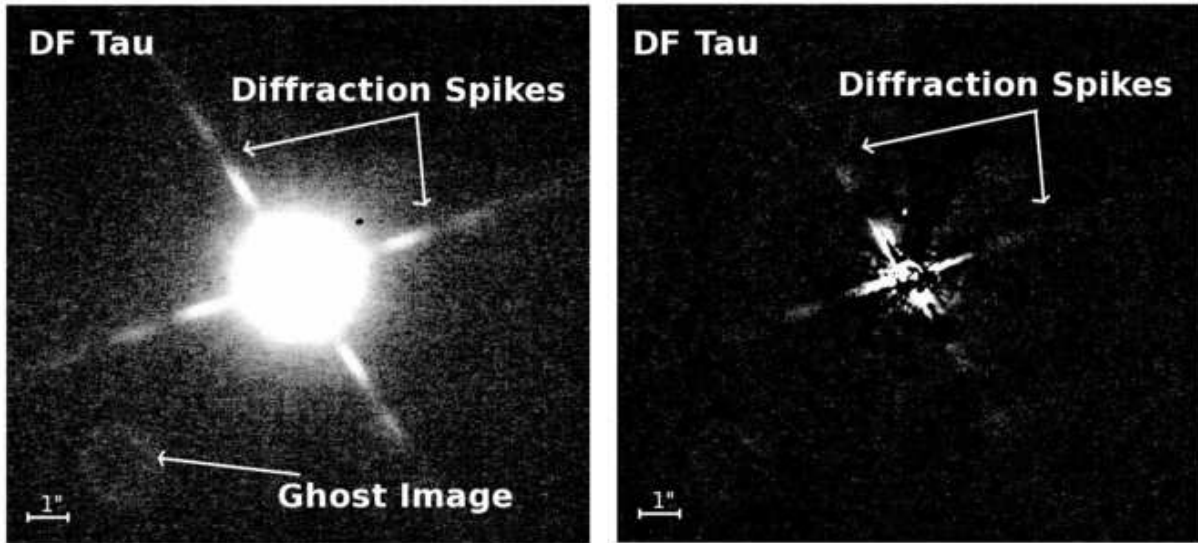


Fig. 1.— Example of a null detection (no extended emission) for DF Tau. The left panel shows the pre PSF subtraction image, with instrumental artifacts labeled. The right panel shows the post subtraction artifacts. Compare with the potential detections of Figure 3.

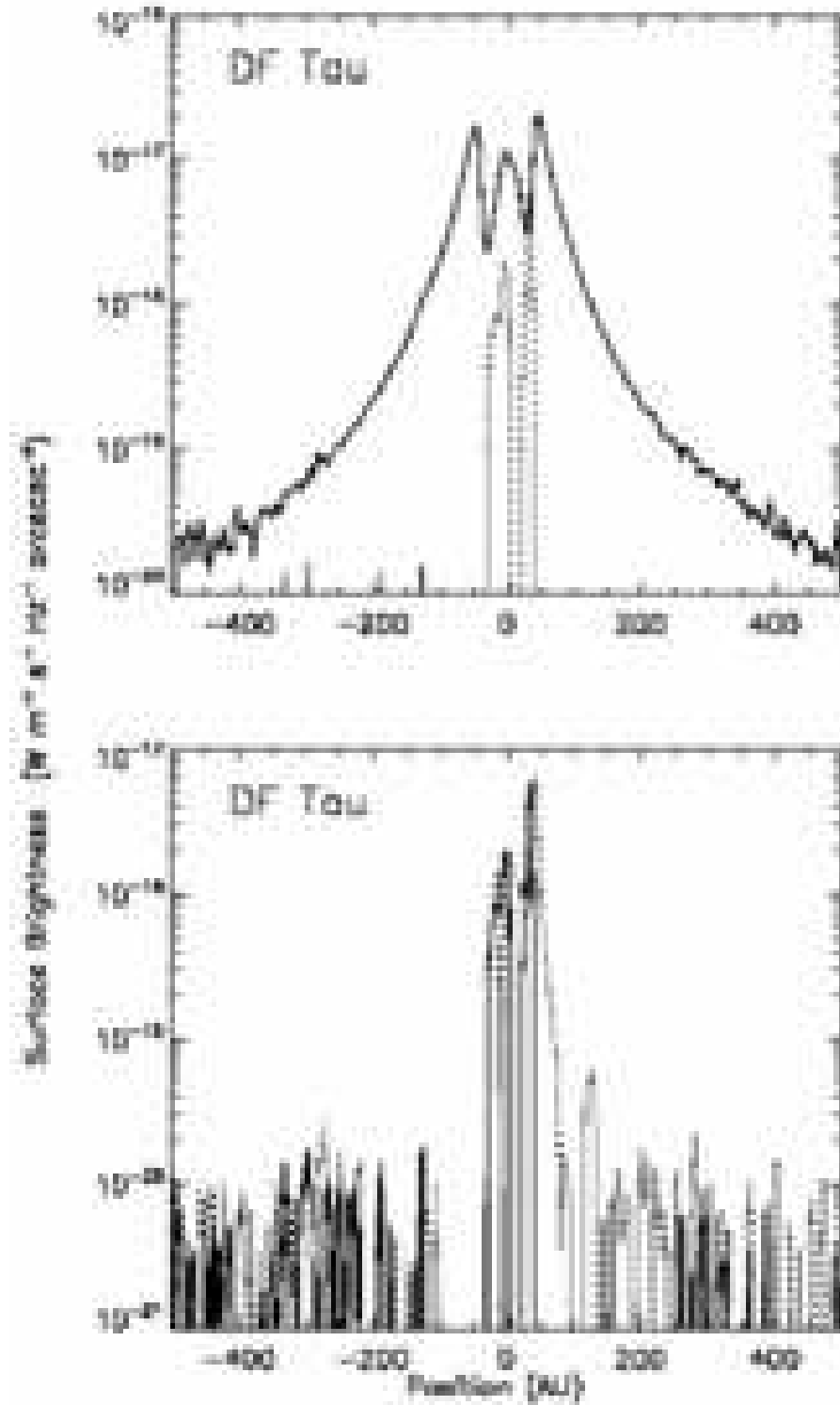


Fig. 2.— Profiles for the non-detection of Figure 1. The top panel shows pre-(solid) and post (dashed) subtraction profiles along an axis off of the diffraction artifacts. The lower panel shows the two post subtraction profiles, perpendicular to each other. Compare with the detections in Figure 4. In all cases the profiles are averaged over seven pixels.

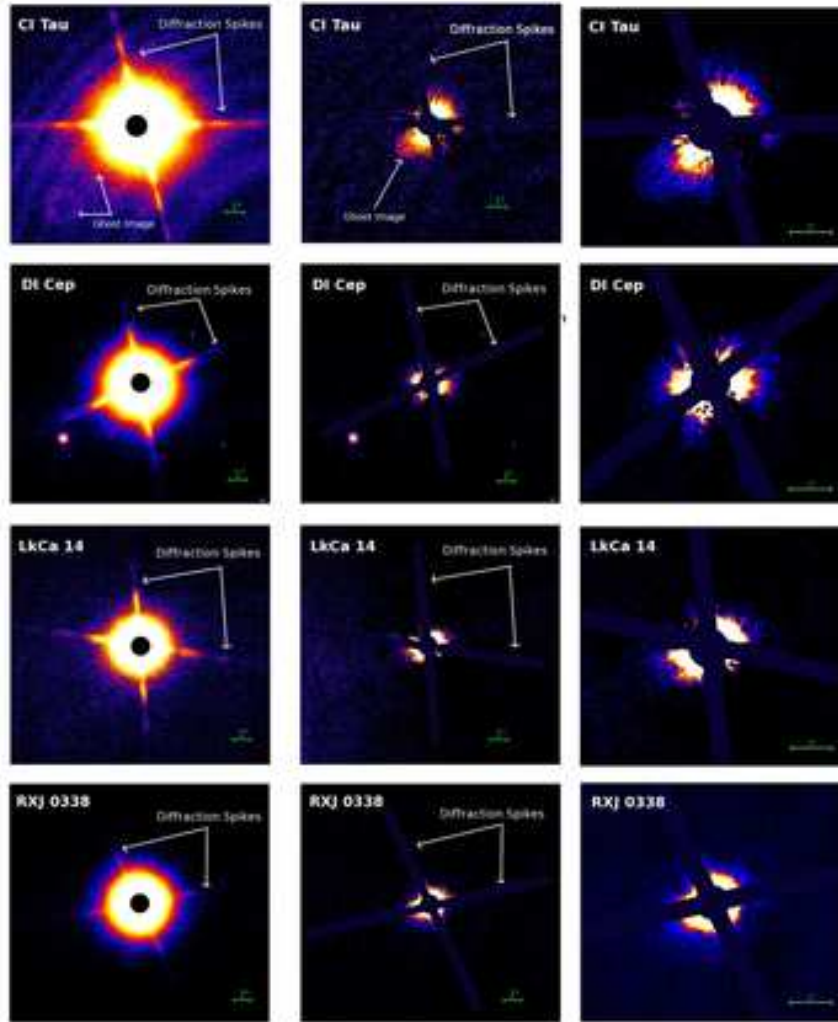


Fig. 3.— Pre-(left) and post (middle,right) subtraction images for all four potential detections. The diffraction patterns are marked, and masked out in the subtracted image; as is the central, artifact dominated region. The ghost image near CI Tau is also indicated. The left and middle panels are on the same physical scale, the right panel shows a close-up of the extended emission.

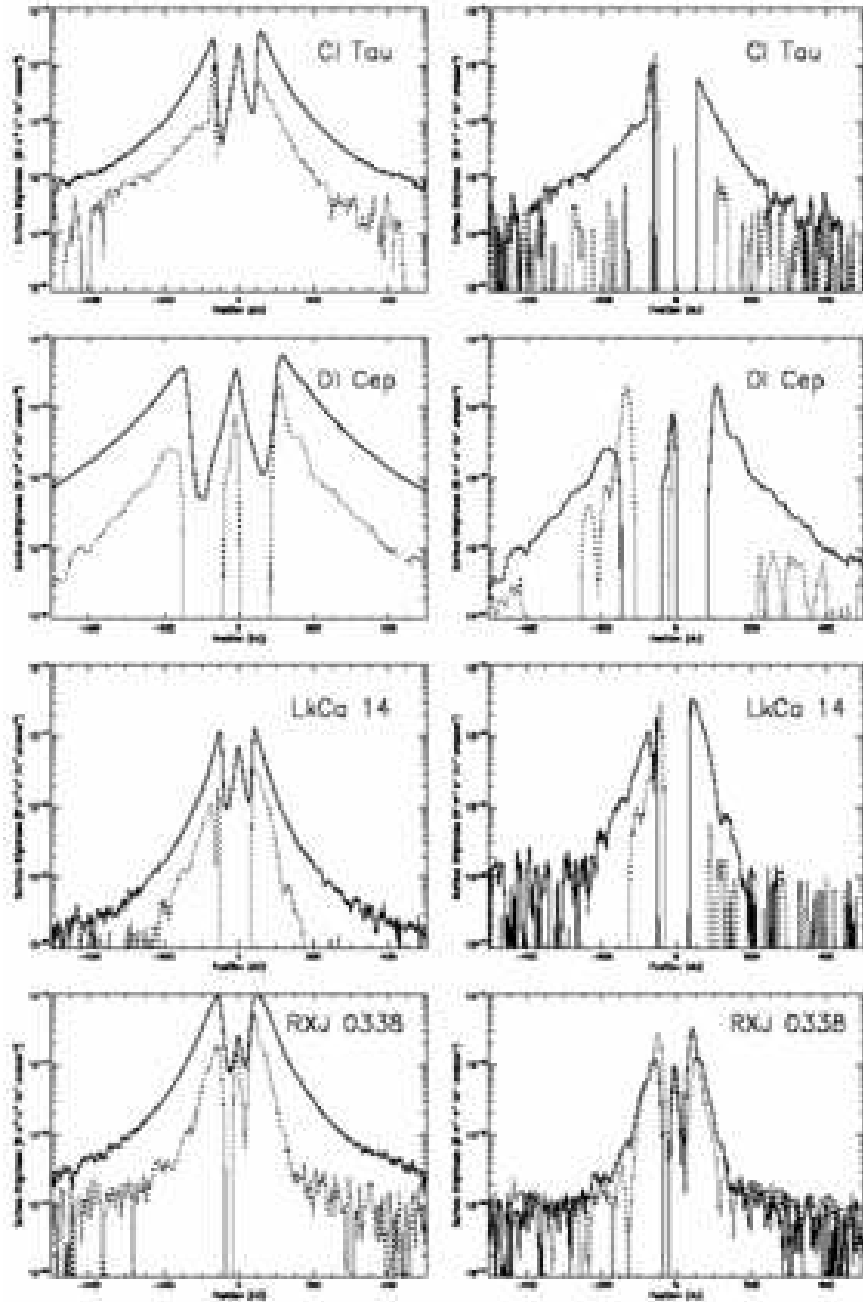


Fig. 4.— Pre-and post PSF subtraction profiles all four potential detections. The left panels show the pre-(solid) and post (dashed) subtraction profiles along the major axis of emission, the right panels show the post subtraction profiles along (solid) and perpendicular to (dashed) the major axis of emission. In all cases the profiles are averaged over seven pixels.



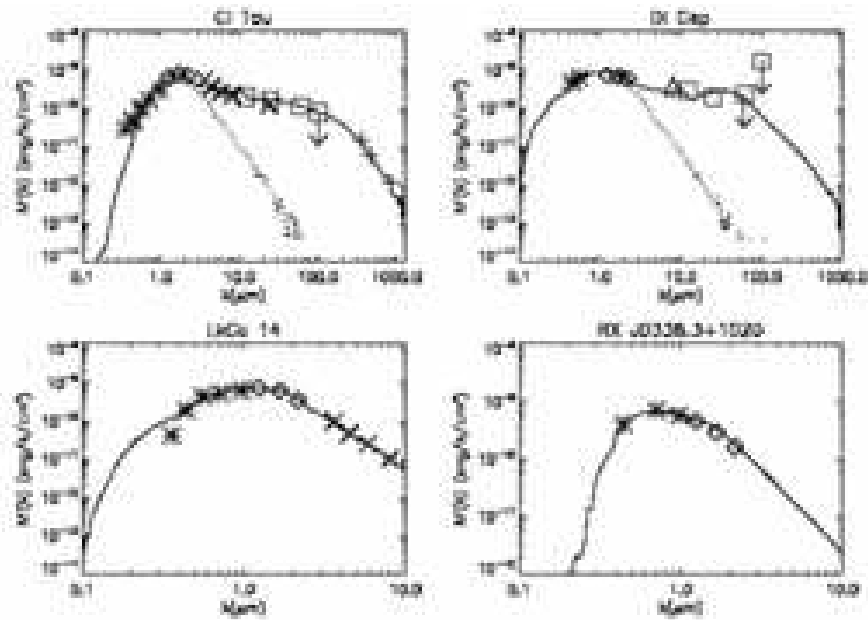


Fig. 5.— SEDs for the tentative detection; Stars; optical photometry (U-I band); Diamonds; 2MASS JHK<sub>s</sub> photometry; Crosses; Spitzer; Squares; IRAS, Pluses; sub-mm/mm data. Upper limits are indicated by downwards arrows. The solid line is the SED from the disk model (Robitaille et al. 2006), the dashed line the component from the stellar black-body only, for the WTTS these are identical.

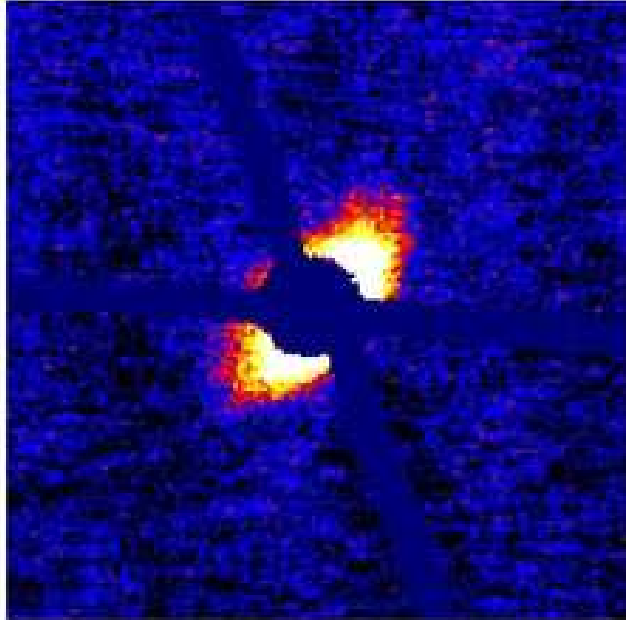


Fig. 6.— Simulated image for a disk which is consistent with the SED of CI Tau, for a disk with a mass of  $0.03 M_{\odot}$  and outer radius of 133 AU, inclination of 63 degrees.

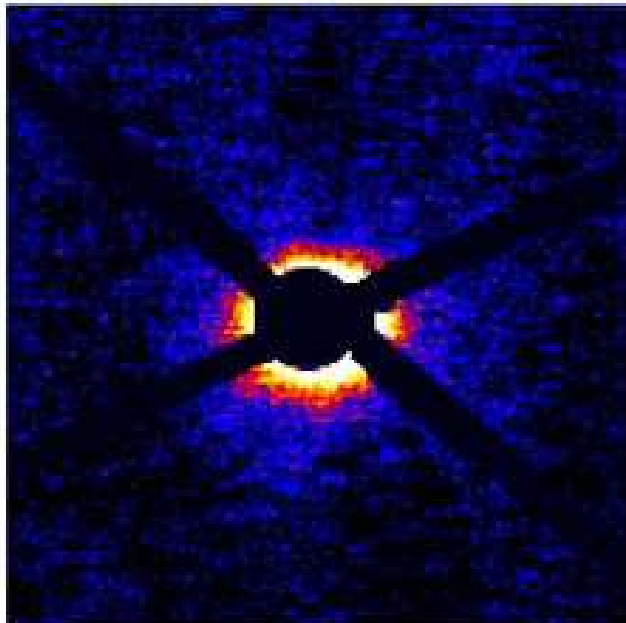


Fig. 7.— Simulated image for a disk which is consistent with the SED of RXJ 0338, for a disk with a mass of  $2.8 \times 10^{-3} M_{\odot}$ , with an inclination of 44 degrees and an inner disk gap of 20 AU radius. The inner disk gap is within the mask, and not visible.

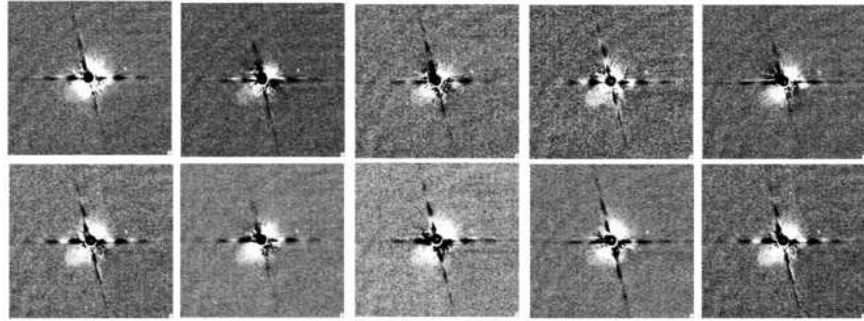


Fig. 8.— Details of the reduction of CI Tau, showing the results of individual frames.

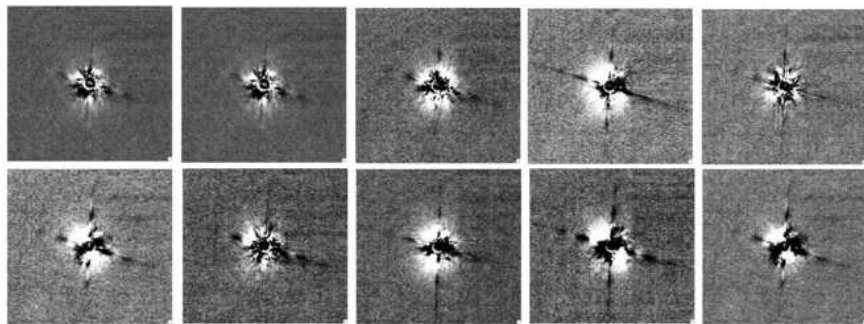


Fig. 9.— Details of a messy null detection which fails the selection process (CW Tau)

Table 1. The Entire Sample

Name	Spectral Type	Evolutionary Status	Name	Spectral Type	Evolutionary Status
CI Tau	GV:e	CTTS	RX J0423.5+0955	K4	WTTS
CW Tau	K5V:e	CTTS	RX J0426.4+0957W		WTTS
DE Tau	M1V:e	CTTS	RX J0438.2+2023	G9	WTTS
DF Tau	K5	CTTS	RX J0445.3+0914	G0	WTTS
DP Tau	M0V:e	CTTS	RX J0512.0+1020	K2	WTTS
DS Tau	K4V:e	CTTS	RX J0528.4+1213	K2	WTTS
FM Tau	K3	CTTS	LkCa 1	M4V	WTTS
GI Tau	K5e	CTTS	LkCa 4	K7:V	WTTS
HO Tau		CTTS	LkCa 5	M2V	WTTS
ZZ Tau IRS	M5.2v	CTTS	LkCa 14	M0:V	WTTS
HBC 347	K1	WTTS	LkCa 19	K0V	WTTS
HBC 366	M0V	WTTS	HD 17543c	F8V	WTTS
HBC 374	K7	WTTS	HD 41593	K0	WTTS
HBC 376	K7	WTTS	V386 Cep	S	WTTS
HBC 388	K1	WTTS	Haro 6-10	K3	Class I
HBC 392	K5	WTTS	BD+31 643	B5	Herbig Be
HBC 397	K7	WTTS	HDE 283572	G2III	WTTS
HBC 403	K7	WTTS	DI Cep	G8V	CTTS
HBC 415	Gn	WTTS	BM And	K5V	CTTS
RX J0336.0+0846	M3	WTTS	V826 Tau	K7Ve	WTTS
RX J0338.3+1020	G9	WTTS	V827 Tau	K7	WTTS
RX J0404.4+0518	K0	WTTS	V830 Tau	K7	WTTS
RX J0409.8+2446	M1.5	WTTS			

Table 2. Observational Parameters

Source	Date Observed	Photometric Reference <sup>1</sup>	Number of Frames Observed	Exposure Time/Frame (s)	PSF Reference
RX J0338.8+1020	2003 Dec 3	FS 120	117	10	SAO 76545
SAO 76545	2003 Dec 3	FS 120	144	10	
CI TAU	2005 Nov 10	FS 125	100	15	SAO 76560
SAO 76560	2005 Nov 10	FS 125	170	12	
LkCa 14	2003 Nov 4	FS 115/FS 4	36	30	HD 286794
HD 286794	2003 Nov 4	FS 115/FS 4	45	30	
DI Cep	2005 Nov 12	FS 125	60	20	SAO 34978
SAO 34978	2005 Nov 12	FS 125	96	10	

<sup>1</sup>UKIRT Faint Spectral Standards (Leggett et al. 2006)

Table 3. Sources with Potential Detections

Object	Spectral Type	Class	RA J2000	Dec J2000	Binary <sup>1</sup>	Comp <sup>2</sup>	Distance pc	5 $\sigma$ Limit (Frame) $\text{Wm}^{-2}\text{s}^{-1}\text{Hz}^{-1}$	5 $\sigma$ Limit (Coadd) $\text{Wm}^{-2}\text{s}^{-1}\text{Hz}^{-1}$	PA E of N	Morphology	Extent
CI Tau	K7	CTTS	04 <sup>h</sup> 33 <sup>m</sup> 52 <sup>s</sup> .0	+22 <sup>o</sup> 50' 30.2"	N	N	140	2.15e-19	1.15e-19	35	Elongated	190 AU
RX J0338.2+1020	G9	WTTS	03 <sup>h</sup> 38 <sup>m</sup> 18 <sup>s</sup> .2	+10 <sup>o</sup> 20' 17.1"	N	N	140	1.57e-18	6.5e-19	–	Symmetrical	190 AU
LkCa 14	M0	WTTS	04 <sup>h</sup> 36 <sup>m</sup> 19 <sup>s</sup> .1	+25 <sup>o</sup> 42' 59.1"	N	N	140	1.04e-19	7.97e-20	45	Elongated	120 AU
DI Cep	G8	CTTS	22 <sup>h</sup> 56 <sup>m</sup> 11 <sup>s</sup> .5	+58 <sup>o</sup> 40' 01.8"	N	Y	300	3.18e-20	1.64e-20	85	Elongated	370 AU

<sup>1</sup>Resolved close binary (within mask)

<sup>2</sup>Faint companion

Table 4. Photometry

Object	U	V	B	R	I	J mag	H	K	3.6	4.5	5.8	8	24	12	25	60	100 mJy	350	450	850	1300	References
LkCa 14	–	12.78	11.51	10.81	–	9.34	8.71	8.58	8.47	8.54	8.49	8.44	–	–	–	–	–	–	–	–	–	1,2,6
CI Tau	14.27	14.42	13.25	12.2	11.1	9.47	8.42	7.8	6.59	6.26	5.94	5.1	2.4	800	1380	2220	2254L	1725	846	324	190	2,3,7,8,10
DI Cep	–	11.9	11.3	–	–	9.3	8.57	7.95	–	–	–	1000	–	1170	1540	4570L	56960L	–	103L	9L	19L	2,4,8,9,10
RXJ 0338	–	13.31	12.012	10.85	9.815	9.452	9.360	–	–	–	–	–	–	–	–	–	–	–	–	–	2,5	

<sup>1</sup>Grankin et al. (2008)

<sup>2</sup>Cutri et al. (2003)

<sup>3</sup>Audard et al. (2007)

<sup>4</sup>Ismailov and Grankin (2007)

<sup>5</sup>Monet et al. (2003)

<sup>6</sup>Hartmann et al. (2005)

<sup>7</sup>Furlan et al. (2006)

<sup>8</sup>Beichman et al. (1988)

<sup>9</sup>Egan et al. (1999)

<sup>10</sup>Andrews and Williams (2005)

This figure "f1.jpg" is available in "jpg" format from:

<http://arxiv.org/ps/0911.5583v1>